



Intensified Kirkendall effect assisted construction of double-shell hollow Cu-doped CoP nanoparticles anchored by carbon arrays for water splitting

Xian Wang^{a,c,1}, Haigen Huang^{b,1}, Jinjie Qian^c, Yingwei Li^a, Kui Shen^{a,*}

^a State Key Laboratory of Pulp and Paper Engineering, School of Chemistry and Chemical Engineering, South China University of Technology, Guangzhou 510640, China

^b College of Chemistry and Chemical Engineering, Jinggangshan University, Ji'an 343000, China

^c College of Chemistry and Materials Engineering, Wenzhou University, Wenzhou 325000, China

ARTICLE INFO

Keywords:

Double-shell hollow nanoparticles
Metal-organic framework
Kirkendall effect
Transition metal phosphide
Water splitting

ABSTRACT

Precisely engineering the architectures of nanoparticles (NPs) to optimize their physicochemical properties and thus electrocatalytic performances are challenging for scientists. Here, we report the controllable construction of solid, hollow, and double-shell hollow metal phosphide NPs anchored by carbon nanosheet arrays on carbon cloth. We demonstrate that Cu doping can intensify the nanoscale Kirkendall effect, which promotes the transformation from solid CuCo to double-shell hollow CoP NPs. Benefiting from its high dispersity, large electrochemical specific surface area, fast mass diffusion and good conductivity, the optimal double-shell hollow Cu-CoP-based electrocatalyst exhibits excellent activities for OER ($\eta_{10} = 176$ mV) and water splitting (1.494 V @ 10 mA) in 1.0 M KOH with favorable stability. DFT calculations further confirm the optimized OH* adsorption energy of Cu-CoOOH/Cu-CoP due to Cu doping and interfacial synergy for boosting OER. This work provides new perspectives for engineering the nanoarchitecture of multilevel hollow NPs through the Kirkendall effect for electrocatalysis.

1. Introduction

Energy crisis and environmental problems are major problems faced by contemporary people in the process of survival and development [1]. Water splitting is a promising energy storage and conversion technology to convert unstable renewable energy such as solar and wind energy into clean hydrogen energy [2,3]. However, the currently commercialized catalysts for water splitting are mainly prepared by noble metals such as platinum [4] and iridium [5], which are expensive, scarce, and thus not conducive to large-scale applications. Therefore, people need to develop efficient, cheap, and abundant non-noble metal-based catalysts to promote the large-scale industry for water splitting [6,7]. Recently, various transition metal phosphide-based materials have been proved to be ideal non-noble metal electrocatalysts for water splitting due to their low cost and high intrinsic activity [8]. Nevertheless, the bulk or solid particle form of these electrocatalysts shows limited mass diffusion and low contact surface area with the reactants, which greatly decelerate their electrocatalytic reaction kinetics [9]. With the development of nanotechnology, the rational design and fabrication of novel nanocatalysts with desired hierarchical architectures have been identified as an ideal

strategy to optimize efficient electrocatalysts [10,11]. Accordingly, controlling the morphology, nanoarchitecture, and composition of transition metal phosphide nanoparticles (NPs) to adjust their unique physical and chemical properties has attracted considerable attention in the fields of nanomaterial science and electrocatalysis [12,13].

Among various nanoarchitectures, hollow NPs are a kind of star material with great application prospects [14] in catalysis [15], drug delivery [16], photoelectromagnetic response [17], and especially in energy storage and conversion [18,19], due to their high surface-to-volume ratio, fast mass diffusion rate, and high atom utilization. People usually use hard-templated [20], soft-templated [21], self-templated [22], etc to prepare various hollow NPs. Among them, the self-templated method is a simple and cost-effective strategy, which is based on the hollowing of the initial solid NPs to hollow NPs through various chemical transformation processes mainly including the Kirkendall effect [23], galvanic replacement [14], and Ostwald ripening [24]. So far the classic Kirkendall effect caused by the difference in the diffusion rate between different anions and cations has been frequently used to synthesize many hollow metal compound NPs, such as metal oxides [25], metal sulfides [26], and metal phosphides [27]. In

* Corresponding author.

E-mail address: cekshen@scut.edu.cn (K. Shen).

¹ These authors contributed equally to this work.

particular, since Chiang et al. synthesized hollow Ni_2P NPs based on the Kirkendall effect [28], different types of hollow phosphide NPs even including noble metal phosphides such as PtP_2 , Rh_2P , Au_2P_3 , Pd_5P_2 , and PdP_2 NPs have been successfully prepared [29]. Although this efficient strategy has proved the extraordinary versatility to prepare various single hollow phosphide NPs, it seems to encounter difficulties in precisely engineering the nanoarchitecture of hierarchical hollow phosphide NPs. Especially, to the best of our knowledge, the construction of multi-shelled hollow metal phosphide NPs based on the Kirkendall effect has never been achieved so far, despite their more attractive properties such as enhanced mass diffusion and favorable multiphase heterogeneous interfaces, as compared with their single-shelled hollow counterparts. Furthermore, the synthesis of metal phosphide NPs based on the Kirkendall effect is usually performed in a liquid solvent and thus the as-obtained NPs in a colloidal form require further separation, purification, and being loaded onto a current collector with a polymer binder when being employed as electrocatalysts [27–29]. These complicated processes are not only time-consuming, but also could result in some unwished problems, such as the increased electronic resistance of catalysts, the coverage of active centers, the blockage of mass transfer channels, and the easy expulsion of catalysts [30]. In addition, they are also prone to agglomerate during the reaction process, reducing the activity and stability of the catalyst [31]. Therefore, directly engineering the nanoarchitecture of hierarchical metal phosphide NPs on a self-supported electrode material is highly attractive for efficient water splitting but still remains a daunting challenge.

Accordingly, herein, we report the first example of constructing leaf-shaped porous carbon arrays loaded with double-shell hollow Cu-doped CoP NPs on carbon cloth (denoted as DH-CuCo-P @ NC/CC) for boosting overall water splitting. We demonstrate that the combination of Cu doping and pre-oxidation enables the transformation from solid CuCo NPs to double-shell hollow Cu-doped CoP NPs. In addition, we also investigate the detailed mechanism for the structural evolution of double-shell hollow Cu-doped CoP NPs, and reveal that Cu doping can intensify the Kirkendall effect in the phosphating process, which is the key to the formation of a double-shell hollow nanostructure. Meanwhile, by changing the composition of metal elements and calcination conditions, we can also precisely control the structure of metal phosphide NPs wrapped in carbon nanosheets, including solid, single-shell hollow, and double-shell hollow nanostructures. Among them, DH-CuCo-P @ NC/CC composed of carbon fibers loaded with carbon nanosheet arrays rich in double-shell hollow Cu-doped CoP NPs is an excellent three-dimensional (3D) self-supported electrocatalyst that can be directly applied to highly-efficient water splitting in an alkaline condition. It is found that the Cu-doped CoP NPs maintain a stable structure after hydrogen evolution reaction (HER), and part of them would be converted into Cu-doped CoOOH after oxygen evolution reaction (OER). Furthermore, theoretical calculations show that Cu doping and the synergistic effect of the Cu-CoOOH/Cu-CoP interface can both improve its OER intrinsic activity.

2. Experimental

2.1. Synthesis of DH-CuCo-P@NC/CC

The purchased carbon cloth is immersed in a mixture of concentrated sulfuric acid and nitric acid for 1 day. The pre-treated carbon cloth is vertically immersed in a mixture of 40 ml aqueous solution of $0.4656\text{ g Co}(\text{NO}_3)_2 \cdot 6\text{H}_2\text{O}$ and $0.0964\text{ g Cu}(\text{NO}_3)_2 \cdot 3\text{H}_2\text{O}$ and 40 ml aqueous solution of 1.312 g 2-MeIM for 4 h at room temperature. The reacted carbon cloth is taken out, washed with deionized water and ethanol 3 times, and vacuum dried at $60\text{ }^\circ\text{C}$ for 12 h to obtain ZIF-L-CuCo/CC. The prepared ZIF-L-CuCo/CC ($1 \times 4\text{ cm}^2$) is placed in an open quartz boat and heated to $800\text{ }^\circ\text{C}$ at a rate of $2\text{ }^\circ\text{C}/\text{min}$ in a tubular furnace for 3 h under the protection of an N_2 atmosphere to get S-CuCo@NC/CC. Then, S-CuCo@NC/CC is oxidized at $250\text{ }^\circ\text{C}$ for 1 h in an oxygen/ N_2 mixed

atmosphere to get YS-CuCo-O@NC/CC. Finally, YS-CuCo-O@NC/CC is transferred to an open quartz boat, and another quartz boat loaded with 160 mg NaH_2PO_2 is placed aside at the upwind in a tubular furnace. And, the tubular furnace is heated to $300\text{ }^\circ\text{C}$ at a rate of $2\text{ }^\circ\text{C}/\text{min}$ for 2 h in N_2 atmosphere to get DH-CuCo-P @ NC/CC.

3. Results and discussion

3.1. Synthesis of nanoparticles with different controllable structures in carbon nanosheets

In the schematic illustration of material synthesis (Fig. 1), we report a strategy of using the Kirkendall effect to control the nanostructure of metal phosphide NPs, including solid, single-shell hollow, and double-shell hollow CoP NPs that are wrapped in the carbon nanosheet arrays on a carbon cloth substrate. First, we acidify the carbon cloth (CC) substrate (Fig. S1) with concentrated acid as a pre-treatment, so that carbon fibers in CC are oxidized to be rich in -OH and -COOH functional groups and become more hydrophilic. Next, in an aqueous solution at room temperature, abundant hydrophilic functional groups on the acid-treated CC can capture Co^{2+} cations after deprotonation [32], which then coordinate with ligands of 2-MeIM to self-assemble leaf-shaped nanosheet arrays of Co-based ZIF-L uniformly loaded on the CC (denoted as ZIF-L-Co/CC) (Fig. S2). Similarly, by partly adding copper nitrate ($\text{Cu}_{\text{mol}}:\text{Co}_{\text{mol}} = 1:4$), Cu^{2+} cations can partially replace Co^{2+} cations to form Cu-doped ZIF-L-CuCo precursor, thereby obtaining ZIF-L-CuCo/CC (Fig. S3). As shown in Fig. S4, the X-ray diffraction (XRD) pattern of ZIF-L-CuCo/CC shows sharper characteristic peaks as compared with that of ZIF-L-Co/CC, indicating that Cu doping can increase the crystallinity of ZIF-L-Co. On the one hand, ZIF-L-Co/CC undergoes a two-step treatment of high-temperature pyrolysis under inert gas protection and phosphating at $300\text{ }^\circ\text{C}$ to get corresponding leaf-shaped carbon nanosheet arrays wrapped with solid CoP NPs on CC (the obtained samples before and after the phosphating process are denoted as S-Co@NC/CC and S-Co-P @ NC/CC, respectively). On the other hand, by using ZIF-L-CuCo/CC as an alternative precursor, the CC carrying carbon nanosheet arrays wrapped with hollow bimetallic phosphide NPs can be prepared after the same process of pyrolysis and phosphating, denoted as H-CuCo-P @ NC/CC (Fig. S5). In addition, S-CuCo@NC/CC can be obtained only by carbonizing ZIF-L-CuCo/CC, which is loaded with carbon nanosheet arrays riched in solid CuCo alloy NPs (Fig. S6). Furthermore, when the solid CuCo alloy NPs in CuCo@NC/CC are mildly oxidized in an oxygen/ N_2 mixed atmosphere at $250\text{ }^\circ\text{C}$ for 1 h, yolk-shell CuCo@ Co_3O_4 NPs with CuCo alloy NPs as cores and Co_3O_4 oxide layers as shells can be formed in carbon nanosheet arrays (denoted as YS-CuCo-O@NC/CC) (Fig. S7). Interestingly, based on a further phosphating process, unique double-shell hollow Cu-doped CoP NPs which are uniformly anchored in the carbon nanosheet arrays on CC can be finally prepared (Fig. S8).

3.2. Comparison of morphologies and structures of various materials

In Fig. 2, scanning electron microscope (SEM) and transmission electron microscope (TEM) are used to compare the microscopic morphologies and structures of S-Co-P @ NC/CC, H-CuCo-P @ NC/CC, and DH-CuCo-P @ NC/CC. From low magnification SEM images (Fig. 2a₁-a₂, b₁-b₂, and c₁-c₂), these three materials are similar. All of them well maintain the morphology of their precursors and can be directly used as self-supported electrocatalysts composed of carbon fibers uniformly assembling leaf-shaped carbon nanosheet arrays. By using the TEM, the microstructure of loaded NPs in carbon nanosheets can be observed more clearly (Fig. 2a₃-a₇, b₃-b₇, and c₃-c₇). In all three materials, metal phosphide NPs are uniformly distributed on the carbonized carbon nanosheets. And, according to high-angle ring darkfield scanning transmission electron microscope (HAADF-STEM) images with the corresponding energy-dispersive X-ray spectrum (EDS) element mapping

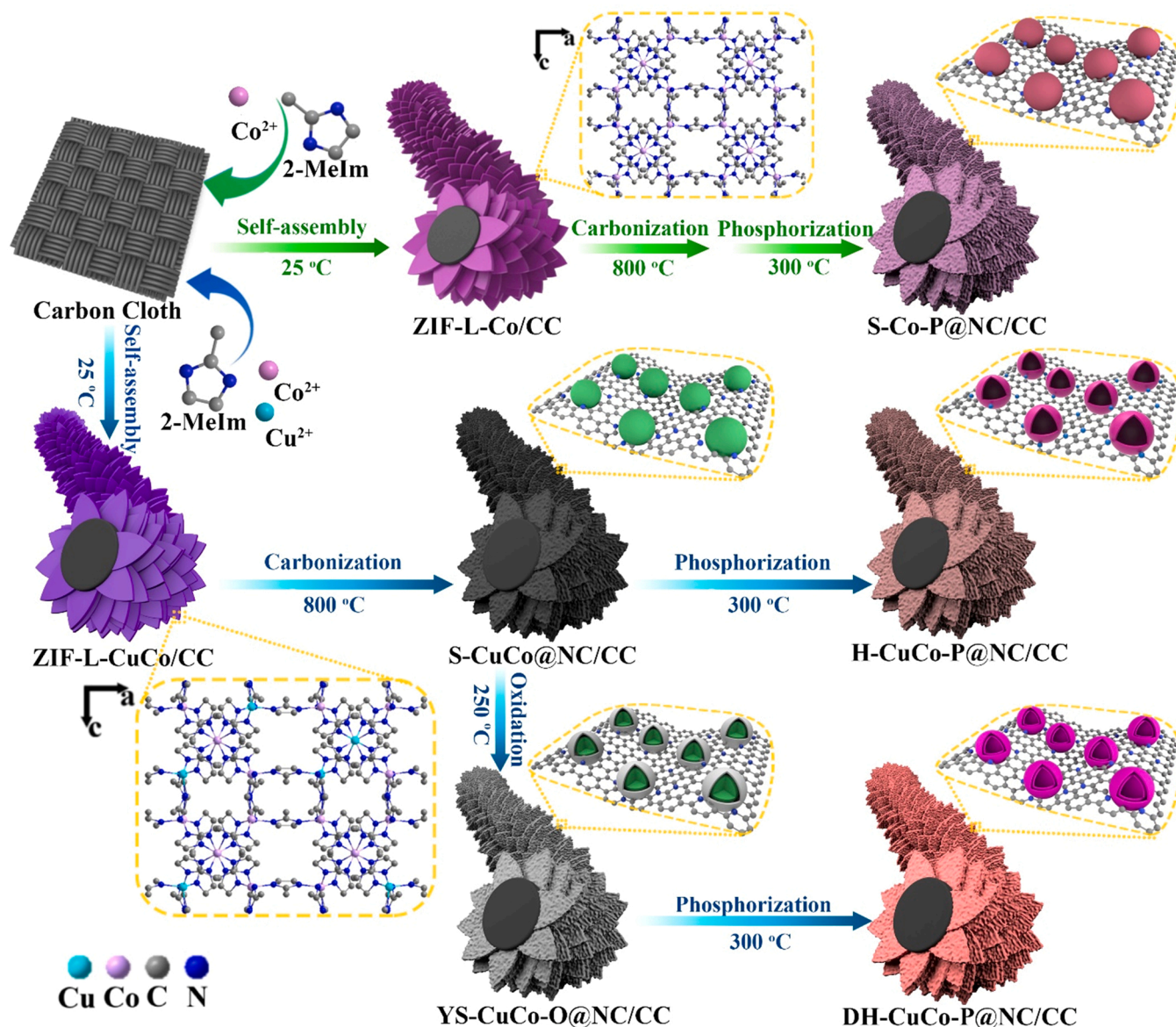


Fig. 1. Schematic illustration of the synthesis of S-Co-P@NC/CC, H-CuCo-P@NC/CC, and DH-CuCo-P@NC/CC composites with different embedded nanoparticles.

images of all three materials, we can find that Co, P, O, and Cu elements are evenly dispersed in the carbon layers, and Co and P elements are concentrated in the range of NPs. The difference is that we can intuitively observe that metal phosphide NPs loaded on S-Co-P @ NC/CC are solid, on H-CuCo-P @ NC/CC are hollow, and on DH-CuCo-P @ NC/CC are double-shell hollow, respectively. In addition, the distributions of Co, P, and Cu elements in both H-CuCo-P @ NC/CC and DH-CuCo-P @ NC/CC are overlapped, which indicates the formation of Cu-doped CoP NPs. In the high-resolution transmission electron microscope (HRTEM) image of Fig. 2a₅, the spacing of lattice fringes is about 0.189 nm belonging to the (211) plane of CoP, indicating the existence of solid CoP NPs in S-Co-P @ NC/CC. In the XRD pattern of S-Co-P @ NC/CC (Fig. S9), the diffraction peaks at 31.6°, 48.1°, and 56.8° can be indexed to the (001), (211), (301) planes of CoP, which further confirm the formation of CoP NPs. In the HRTEM image of H-CuCo-P @ NC/CC (Fig. 2b₅), a lattice fringe width of 0.221 nm belonging to the (112) plane of Co₂P and a lattice fringe width of 0.248 nm belonging to the (111) plane of CoP can be observed, suggesting that Co₂P and CoP coexist in this sample. These results are also in good agreement with the XRD pattern of H-CuCo-P @ NC/CC in Fig. S10, in which the

characteristic peaks belong to the coexistent Co₂P and CoP. As for Fig. 2c₅, the representative double-shell NP in DH-CuCo-P @ NC/CC demonstrates the 0.248 nm and 0.189 nm lattice spacings, which are corresponding to the CoP (111) and (211) planes, respectively. Through EDS elemental analysis of a representative double-shell hollow Cu-doped CoP NP in Fig. S8m, the element contents of Co, Cu, and P are determined to be 39.2 at%, 3.7 at%, and 39.8 at%, respectively.

In addition, when the above carbonization, oxidation, and phosphating processes are performed by using ZIF-L-Co/CC as a precursor, we can only prepare uneven single-shelled hollow CoP NPs anchored on carbon nanosheet arrays (denoted as H-Co-P @ NC/CC) without Cu doping (Fig. S11). According to TEM and EDS element mapping images of H-Co-P @ NC/CC (Fig. S11d-l), the distributions of Co and P elements are overlapped with the NPs, and these CoP NPs are hollow. The lattice fringes with a spacing of 0.188 nm and 0.247 nm in Fig. S11f can be attributed to the (211) and (111) planes of CoP, which are consistent with the diffraction peaks of CoP of H-Co-P @ NC/CC in Fig. S12.

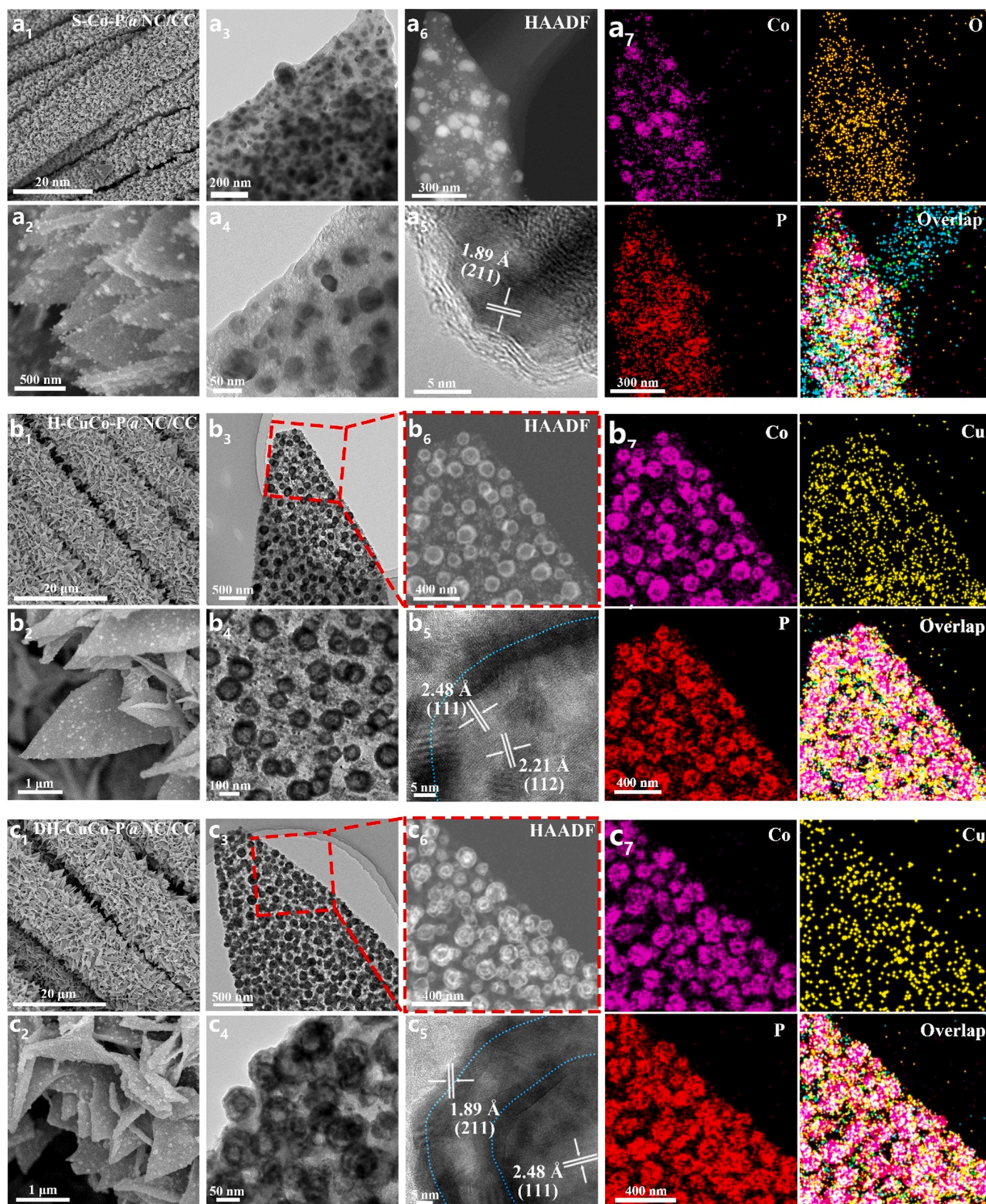


Fig. 2. Comparison of the morphologies and structures of S-Co-P@NC/CC, H-CuCo-P@NC/CC, and DH-CuCo-P@NC/CC. (a₁-a₂) SEM, (a₃-a₅) TEM, (a₆) HAADF-STEM, and (a₇) the corresponding elemental mapping images of Co, Cu and P elements of S-Co-P@NC/CC. (b₁-b₂) SEM, (b₃-b₅) TEM, (b₆) HAADF-STEM, and (b₇) the corresponding elemental mapping images of Co, Cu, and P elements of H-CuCo-P@NC/CC. (c₁-c₂) SEM, (c₃-c₅) TEM, (c₆) HAADF-STEM, and (c₇) the corresponding elemental mapping images of Co, Cu, and P elements of DH-CuCo-P@NC/CC.

3.3. Formation mechanism of the double-shell hollow structure

However, the formation process and mechanism of the double-shell hollow structure of the Cu-doped CoP NP in DH-CuCo-P @ NC/CC is unclear currently and thus worth exploring. To better explain the formation mechanism of the double-shell hollow structure, the formation mechanism of the simpler single-shell hollow NPs in the H-CuCo-P @ NC/CC should be first investigated. Thus, we have explored the structural evolution from S-CuCo@NC/CC to H-CuCo-P @ NC/CC as a function of phosphating time. The time-dependent TEM images and structural evolution diagram are shown in Figs. 3a-e and S13, which demonstrate that CuCo alloy NPs in S-CuCo@NC/CC have undergone a three-step evolution process from the aggregation of irregular NPs to the formation of yolk-shell NP, and finally to the formation of hollow NP. In Figs. 3b and S6, raw CuCo alloy NPs in S-CuCo@NC/CC show an irregular shape and a wide size distribution with the presence of many very small NPs, which are much more uneven than the eventually formed hollow Cu-doped CoP NPs (Figs. 3e and S5). After the phosphating treatment for 30, 60, and 120 min, the elemental mapping images in Fig. 3c₂, d₂, e₂, and the elemental line scan profiles in Fig. S13c-e show that Co and P elements in the cores of these NPs do not overlap for both of the resultant H-CuCo-P @ NC/CC-30 and H-CuCo-P @ NC/CC-60. Until the phosphating time is further increased to 120 min, the Co and P elements in the obtained hollow NPs of H-CuCo-P @ NC/CC are overlapped well. These results reveal that no metal phosphide is formed in the core and the P element gradually diffuses from outside to inside while the CuCo alloy core gradually shrinks until disappears. In step I of the aggregation of NPs, the outermost CuCo alloy can first react with PH₃ derived from the decomposed NaH₂PO₂ to form a thin layer of bimetallic phosphide on the surface. Meanwhile, adjacent small CuCo alloy NPs are more likely to completely react with PH₃ to form small bimetallic phosphide NPs. Consequently, the surface energy of newly formed small metal phosphide NPs is relatively large, and thus they are unstable and tend to adhere to the surface of larger NPs to reduce their surface energy, resulting in the aggregation of NPs. In addition, the NPs reformed from the agglomeration of raw irregular shape NPs or a few medium NPs will tend to be spherical to further reduce their surface energy and be more stable [33,34]. In step II to form yolk-shell NP, the surface CuCo alloy layer has completely reacted with PH₃, and the outward diffusion rate of metal Co and Cu ($D_{\text{Cu}}+D_{\text{Co}}$) is faster than the inward diffusion rate of P (D_{P}), resulting in the intensified Kirkendall effect [28,30]. Therefore, vacancies generate inside the NP, and agglomerate to form internal voids. The further merger of these voids causes the separation of the outer layer of metal phosphide and the inner layer of CuCo alloy core to form a void-rich layer, leading to form the core-shell structure. However, during the formation of the void-rich layer, some voids can merge in advance leading to the phase separation of the metal core and metal phosphide shell, while in some areas of the core and shell are still connected and not completely separated [35, 36]. These remaining junction points can serve as bridges between the core and shell to transport Co and Cu atoms into the shell, which subsequently react with PH₃ to increase the thickness of the outside shell of metal phosphides. Finally, in step III, the Co and Cu atoms in the CuCo alloy core are continuously transported out to form new phosphides in the shell, causing the core to gradually shrink until disappears, forming more vacancies and voids, leading to the collapse of junction points and eventually forming a stable spherical hollow Cu-doped CoP NP [37].

Based on the formation process of single-shell hollow CoP NPs in H-CuCo-P @ NC/CC, we can better understand the formation mechanism of double-shell hollow Cu-doped CoP NPs in DH-CuCo-P @ NC/CC. As shown in Figs. 3f-k and S14, the CuCo alloy NPs in S-CuCo@NC/CC have undergone a 4-step evolution process from the aggregation and surface oxidation of irregular NPs, to the formation of yolk-shell NPs, then to the formation of yolk-double-shell NPs, and finally to the formation of double-shell hollow NPs. The lattice fringes with a width of 0.205 nm in Fig. S6f can be assigned to the (111) plane of Co, which confirms that

these dispersed irregular NPs with a smaller particle size are CuCo alloy NPs (Fig. 3g). After the pre-oxidation process of step I (Fig. 3h and S7), the obtained YS CuCo-O@NC/CC shows the uniform distribution of Co, Cu, and O elements in its structure. In the HRTEM image of YS-CuCo-O@NC/CC (Fig. S7f), the lattice fringes with a width of 0.244 nm on the shell can be attributed to the (311) plane of Co₃O₄, and the lattice fringes with a width of 0.205 nm on the core can be assigned to the (111) plane of Co, confirming that the obtained partially-oxidized NPs have a spherical yolk-shell structure. This pre-oxidation process is similar to steps I and II in the phosphating process of H-CuCo-P @ NC/CC. In this pre-oxidation process, the newly formed small CoO_x NPs with relatively large surface energy tend to agglomerate on large NPs to form core-shell CuCo@oxide nanospheres to reduce the surface energy. And then the more outward diffusion of Co and Cu atoms and the insufficient inward diffusion of O atoms can cause a negative flux, resulting in the gradual formation of the first void layer between the CuCo alloy and the oxide layer due to the Kirkendall effect, which will eventually lead to the separation of the core and shell and thus the formation of YS-CuCo-O@NC/CC (Figs. 3h and S15). Subsequently, in step II, the external oxide layer is firstly phosphorized by PH₃ to form metal phosphides. As demonstrated in Fig. 3i, the CuCo alloy in the core would shrink due to the phosphating process, but the EDX element mapping images of Co, Cu, and P reveal that the interior of the CuCo alloy core has not been phosphorized. In step III, a further Kirkendall effect will occur in the phosphatization of the CuCo core. After completely phosphating on the surface of the CuCo core, the internal Cu and Co atoms continue to transport outward and P atoms transport inward to form a new phosphide layer with the formation of many cavities, which leads to forming the second void layer and thus the yolk-double-shell structure of CuCo-P @ NC/CC-60 (Figs. 3j and S16). In the final step IV, the continued phosphatization makes the CuCo alloy in the core completely react until it disappears, and the voids can be merged to collapse the junction points that are originally used as the bridges to connect the core with shells, thereby producing desired double-shell hollow Cu-doped CoP NPs that are uniformly anchored on the carbon nanosheet arrays (Figs. 3k and S8). Additionally, as shown in Fig. 3i-k, the element mapping images of Co, Cu, and P reveal that the core of the CuCo alloy has not been totally phosphating until it disappears. It is also consistent with the corresponding element line scanning images (Figs. 3e-f and S14d), which suggests that the content of the P element increases with the progress of phosphating.

It is obvious that the Cu-doped CoP NPs in H-CuCo-P @ NC/CC and DH-CuCo-P @ NC/CC has an additional hollow layer as compared with the CoP NPs in S-Co-P @ NC/CC and H-Co-P @ NC/CC prepared under the same pyrolysis conditions, respectively. Therefore, we speculate that Cu doping plays a key role in the preparation of H-CuCo-P @ NC/CC and DH-CuCo-P @ NC/CC. As shown in Fig. 3g₂, h₂, i₂, j₂, and k₂, Cu atoms are more dispersed than Co atoms in the preparation process of DH-CuCo-P @ NC/CC., which implies that the diffusion rate of Cu is faster than that of Co during this process. Generally, in the early stage of this phosphating process, there are fewer P atoms and metal atoms as possible [38]. One P atom can form Co₂P with two Co atoms [12], but to form Cu₃P needs three Cu atoms [39], which will bring about a larger negative flux. Thus, we believe that the introduction of Cu can greatly increase the void generation speed in the early stage of phosphating, which intensifies the Kirkendall effect, thereby accelerating the void layer formation and favoring the hollow structure formation for H-CuCo-P @ NC/CC and DH-CuCo-P @ NC/CC. And, due to the effect of small-nanoparticle agglomeration and reorganization, it is understandable that the Kirkendall effect which occurs in the formation of S-CoP@NC/CC with a not strong enough negative flux between D_{Co} and D_{P} fails to produce a large enough void layer for the formation of the hollow structure during the phosphating process, resulting in the solid CoP NPs in S-Co-P @ NC/CC. Similarly, the single-hollow CoP NPs in H-Co-P @ NC/CC are only caused by the phosphating of the outer oxide layer of Co NPs in the pre-oxidized S-Co@NC/CC sample.

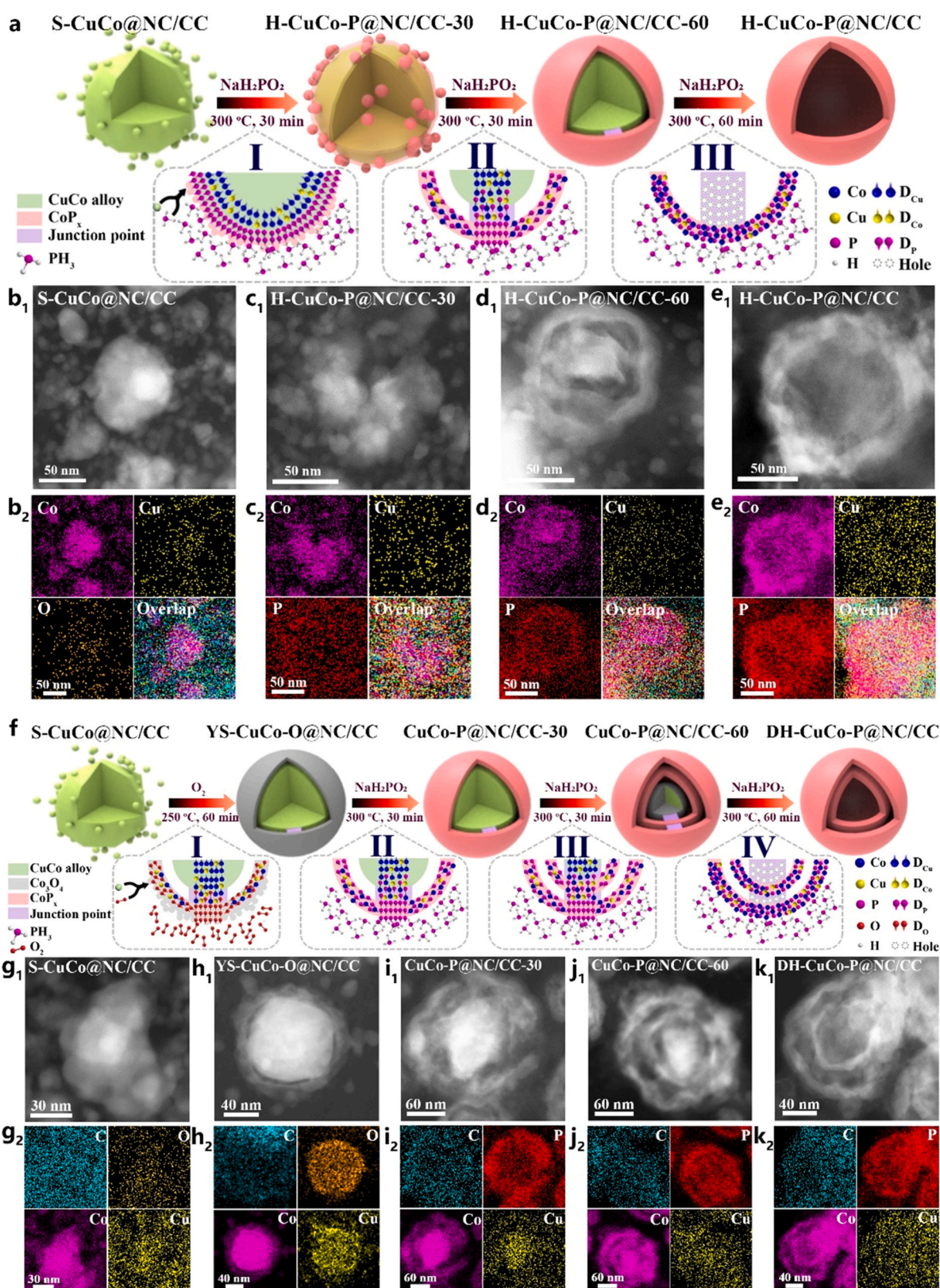


Fig. 3. Morphological and structural evolution of nanoparticles during transformation. (a) Mechanistic diagram of transformation from solid to hollow nanoparticles; (b₁-b₂), (c₁-c₂), (d₁-d₂), and (e₁-e₂) HAADF-STEM and the elemental mapping images of a selected nanoparticle in S-CuCo@NC/CC, H-CuCo-P@NC/CC-30, H-CuCo-P@NC/CC-60, and H-CuCo-P@NC/CC, respectively. (f) Mechanistic diagram of transformation from solid to double-shell hollow nanoparticles; (g₁-g₂), (h₁-h₂), (i₁-i₂), (j₁-j₂), and (k₁-k₂) HAADF-STEM and the elemental mapping images of a selected nanoparticle in S-CuCo@NC/CC, YS-CuCo-O@NC/CC, CuCo-P@NC/CC-30, CuCo-P@NC/CC-60, and DH-CuCo-P@NC/CC, respectively.

3.4. Spectroscopic characterizations of the structural evolution of DH-CuCo-P@NC/CC

Using other spectroscopic characterizations as supplementary characterization methods, the evolution of DH-CuCo-P @ NC/CC can be disclosed more comprehensively. In Fig. 4a, the obvious characteristic peak at 26.2° for all materials can be assigned to the diffraction peak of the C (002) plane. The XRD pattern of S-CuCo@NC/CC shows two sharp characteristic peaks at 44.2° and 51.5° corresponding to the (111) and (200) planes of Co, respectively, indicating the existence of CuCo alloy in this sample. After a mild pre-oxidation process, the diffraction peaks of the resultant YS-CuCo-O@NC/CC cannot match those of Co_3O_4 , but we can find that the diffraction peaks of metal Co are attenuated by the partial oxidation of CuCo alloy NPs. Furthermore, after the phosphating process, by comparing the characteristic peaks of Co_2P and CoP (Fig. 4a), we find that Co_2P mainly exists in CuCo-P @ NC/CC-30, and

Co_2P and CoP coexist in CuCo-P @ NC/CC-60, while CoP mainly exists in DH-CuCo-P @ NC/CC. These results reveal that in the early stage of phosphating, a small amount of P tends to combine with more Co to form Co_2P . Then, with the increase of the P content and the consumption of metal Co, the phase of Co_2P would transform into CoP. The Raman spectrum of YS-CuCo-O@NC/CC in Fig. 4b shows four characteristic peaks at 467 , 510 , 600 , and 667 cm^{-1} , which can be assigned to the E_g , F_{2g}^2 , F_{2g}^1 , and A_{1g} vibration modes of Co_3O_4 [40], indicating the formation of Co_3O_4 . In addition, the Raman spectra of all samples have two distinct characteristic peaks at ~ 1340 and 1580 cm^{-1} [24], which can correspond to the D peak of defective carbon and the G peak of graphitized sp^2 carbon, respectively. Their intensity ratios of D/G are all around 1.07, suggesting that the degree of graphitization of carbon in these samples are similar and the carbon layers remain stable after the phosphating and oxidation processes.

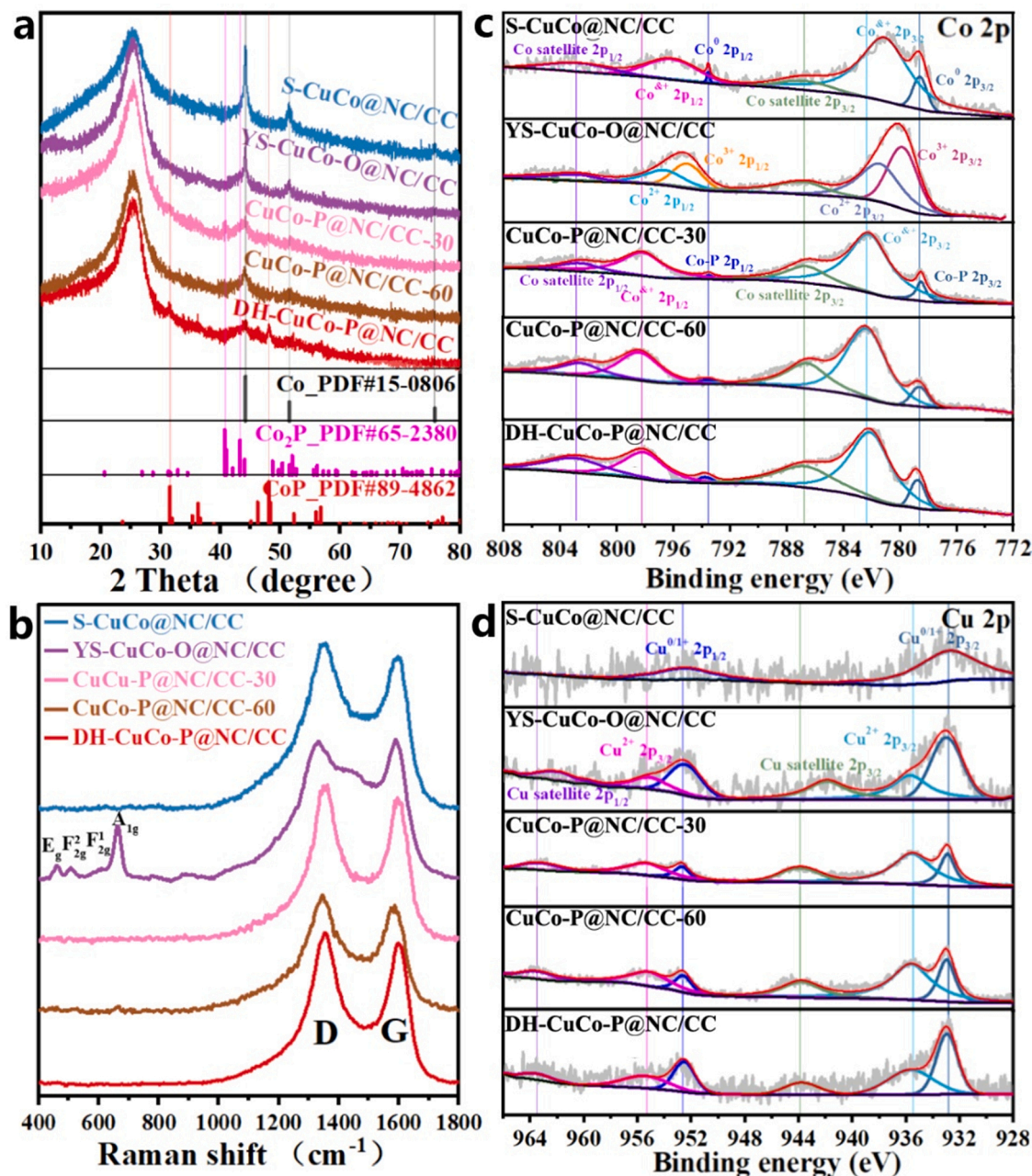


Fig. 4. The structure characterizations of S-CuCo@NC/CC, YS-CuCo-O@NC/CC, CuCo-P@NC/CC-30, CuCo-P@NC/CC-60, and DH-CuCo-P@NC/CC. (a) PXRD patterns, (b) Raman spectra, and high-resolution XPS spectra of (c) Co 2p and (d) Cu 2p for various materials.

X-ray photoelectron spectroscopy (XPS) can be used to further analyze the element compositions and electronic properties of various samples. As shown in Fig. 4c, two obvious peaks at 778.6 and 793.6 eV belonging to the $\text{Co}^{0} 2p_{3/2}$ and $2p_{1/2}$ peaks reveal the existence of CuCo alloy in S-CuCo@NC/CC [24]. In the high-resolution Co 2p XPS spectrum of YS-CuCo-O@NC/CC, the two broad peaks for oxidized Co at around 780 and 795 eV can be further subdivided into four peaks corresponding to the $2p_{3/2}$ and $2p_{1/2}$ peaks of Co^{3+} and Co^{2+} , which are mainly derived from the outer layer of Co_3O_4 [23]. Moreover, as shown in Fig. S17, in addition to C-O and C-O-H bonds, there is also an extra peak representing Co-O and Cu-O bonds at 529.7 eV, which further confirms the presence of an oxidized outer layer on CuCo alloy [41]. For Co satellite $2p_{3/2}$ and $2p_{1/2}$ peaks, they are located at 786.7 and 802.7 eV (Fig. 4c). As for CuCo-P @ NC/CC-30, CuCo-P @ NC/CC-60, and DH-CuCo-P @ NC/CC, the Co-P $2p_{3/2}$ and $2p_{1/2}$ peaks are located at 778.6 and 793.6 eV belonging to the formed Co_3P [42]. The peak area of Co-P peaks is increased from 4.5% (CuCo-P @ NC/CC-30) to 8.3% (DH-CuCo-P @ NC/CC), indicating the phosphatization degree of these materials is deepened. Furthermore, in their high-resolution XPS spectra for P 2p (Fig. S18), the peak area of P $2p_{3/2}$ and $2p_{1/2}$ peaks at 129.9 and

130.8 eV corresponding to Cu-P and Co-P bonds increases, also signing the further formation of Cu-doped CoP. Then, for Cu 2p of these samples (Fig. 4d), the peaks of $\text{Cu}^{0/1} 2p_{3/2}$ and $2p_{1/2}$ are located at 932.9 and 952.5 eV, representing 0, +1 valent Cu and Cu-P bond [43]. Compared with S-CuCo@NC/CC-30, there are more obvious Cu satellite peaks and Cu^{2+} peaks in the spectrum for Cu 2p of YS-CuCo-O@NC/CC, indicating that Cu is further oxidized [44]. And, the increase in the ratio of the $\text{Cu}^{0/1} 2p_{3/2}$ peak area at 932.9 eV also proves the deepening phosphatization degree of DH-CuCo-P @ NC/CC compared with CuCo-P @ NC/CC-30. In addition, in Fig. S19a, the full survey of DH-CuCo-P @ NC/CC exhibits the characteristic peaks of C, N, O, P, Co, and Cu, signing the existence of these elements. For the C1s spectrum of DH-CuCo-P @ NC/CC, the four main peaks at 284.8, 286.0, 288.2, and 290.6 eV are C-C/C=C, C-N/C-O, C=N/C=O, and C satellite peaks (Fig. S19b) [24]. The five peaks of pyridinic-N, Co-N/Cu-N, pyrrolic-N, graphitic-N, and Oxidized-N are located at 398.4, 399.1, 400.0, 401.2, and 403.0 eV (Fig. S19c) [45]. In Fig. S19d, the XPS spectrum for O 1s is divided into the peak of C-O at 531.5 eV and the peak of C-O-H at 533.0 eV. These high-resolution XPS spectra indicate bonding and coordination modes of C, N, and O elements in DH-CuCo-P @ NC/CC

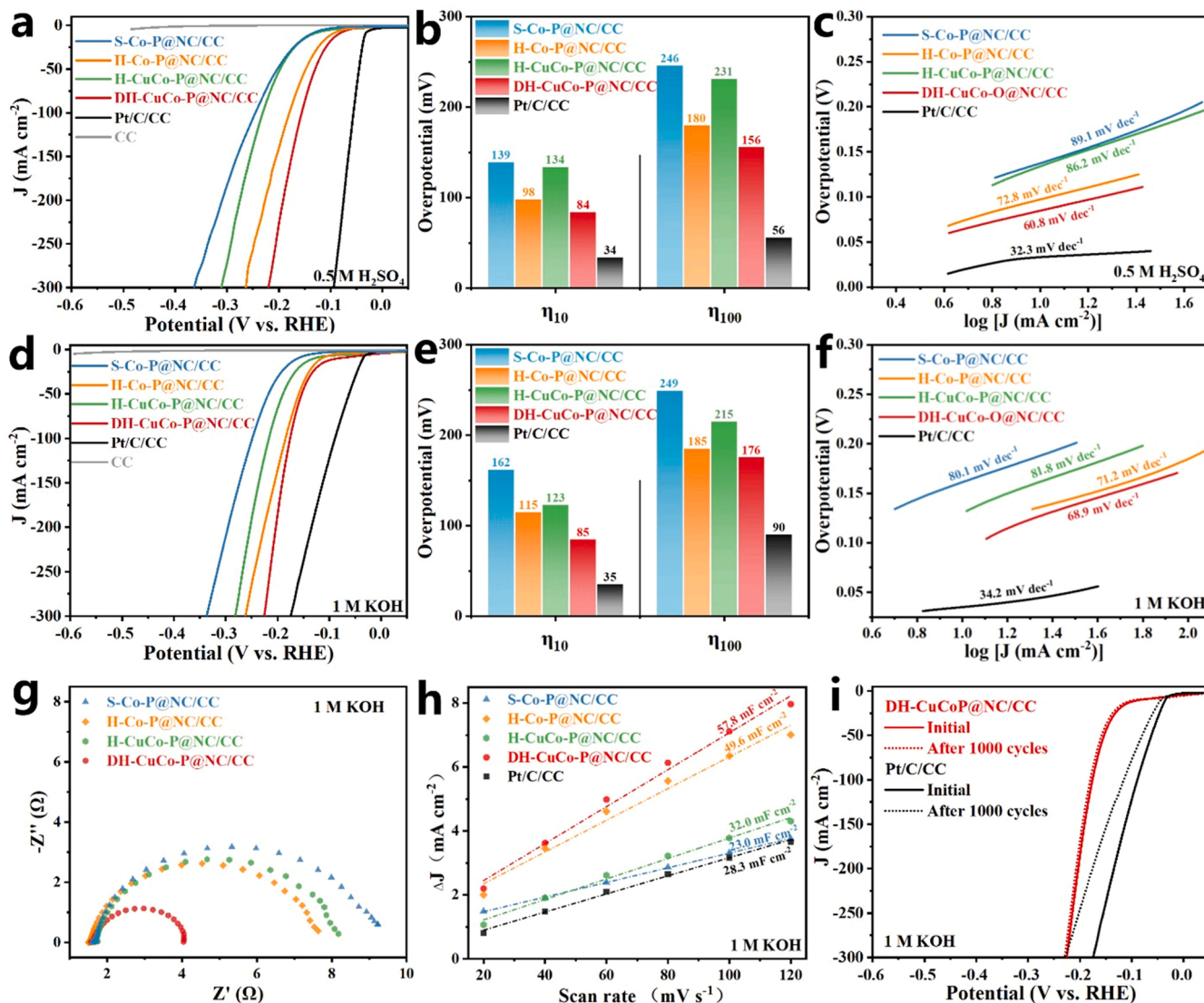


Fig. 5. Electrochemical performances of various electrocatalysts for HER. (a) LSV curves, (b) comparison of η_{10} and η_{100} , and (c) the corresponding Tafel slopes of various electrocatalysts in 0.5 M H_2SO_4 solution for HER. (d) LSV curves, (e) comparison of η_{10} and η_{100} , (f) the corresponding Tafel slopes, (g) EIS Nyquist plots, and (h) capacitive currents at 0.74 V vs. various scan rates of various electrocatalysts in 1 M KOH solution for HER; (i) LSV curves of DH-CuCo-P@NC/CC and Pt/C before (solid lines) and after (dashed lines) accelerated aging test.

(Fig. S19b-d).

3.5. HER performance of electrocatalysts

A standard 3-electrode system is used to evaluate the HER/OER performances of DH-CuCo-P @ NC/CC. S-Co-P @ NC/CC, H-Co-P @ NC/CC, H-CuCo-P @ NC/CC, commercial Pt/C, Ir/C/, and blank CC are used as comparative catalysts. The reference electrode is calibrated with respect to the reversible hydrogen electrode (RHE) (Fig. S20). In all linear sweep voltammetry (LSV) curves of these samples, the CC as a blank control group has almost no current response (Fig. 5a, d). In both acidic and alkaline media for HER (Fig. 5a, b, d, e), DH-CuCo-P @ NC/CC performs superior HER activity with overpotentials at a current density of 10 mA cm^{-2} (η_{10}) of 84 mV in 0.5 M H_2SO_4 and 85 mV in 1 M KOH, which are second only to those of commercial Pt/C (34 and 35 mV, respectively). The HER activities of the comparative phosphide-contained composites are decreased in the following order: H-Co-P @ NC/CC (η_{10} = 98 and 115 mV), H-CuCo-P @ NC/CC (η_{10} = 123 and 134 mV), and S-Co-P @ NC/CC (η_{10} = 139 and 162 mV) in 0.5 M H_2SO_4 and 1 M KOH, respectively. Meanwhile, the corresponding Tafel slopes of DH-CuCo-P @ NC/CC for HER are calculated to be 60.8 mV dec^{-1} in 0.5 M H_2SO_4 and 68.9 mV dec^{-1} in 1 M KOH, both of which are the lowest in this series of phosphide-contained composites (Fig. 5c, f). This

indicates that the rate-determining step of DH-CuCo-P @ NC/CC for HER is hydrogen desorption [46], and DH-CuCo-P @ NC/CC has the most favorable HER kinetics among various phosphide-contained composites. To further assess the charge-transfer kinetics of various electrocatalysts, electrochemical impedance spectroscopy (EIS) is also recorded and the results are shown in Fig. 5a and S21b. Obviously, DH-CuCo-P @ NC/CC demonstrates the smallest charge-transfer resistance (R_{ct}) of 1.0Ω in 0.5 M H_2SO_4 and 2.4Ω in 1 M KOH, suggesting its fast interfacial charge-transfer kinetics for HER [47]. In addition, as shown in Figs. 5h and S22–23, the electrochemical double-layer capacitance (C_{dl}) is calculated based on cyclic voltammetry (CV) curves in the range of $20\text{--}120 \text{ mV s}^{-1}$ for all studied samples. The C_{dl} of DH-CuCo-P @ NC/CC is 56.8 mF cm^{-2} in 0.5 M H_2SO_4 and 57.8 mF cm^{-2} in 1 M KOH, showing the highest electrochemical active surface area (ECSA) in this series of phosphide-contained electrocatalysts due to its more abundant catalytic sites. By contrasting the C_{dl} with η_{10} of various phosphide-contained composites, it can be inferred that the larger the ECSA of the phosphide-contained composites, the higher the activity of HER. According to the LSV curves normalized by ECSA in 0.5 M H_2SO_4 or 1 M KOH solution for HER in Fig. S28a–b, we do not find the obvious positive effect of Cu doping in CoP on enhancing the intrinsic activity for HER. Therefore, the ECSA is the most important factor to affect the HER activity of the as-obtained phosphide-contained

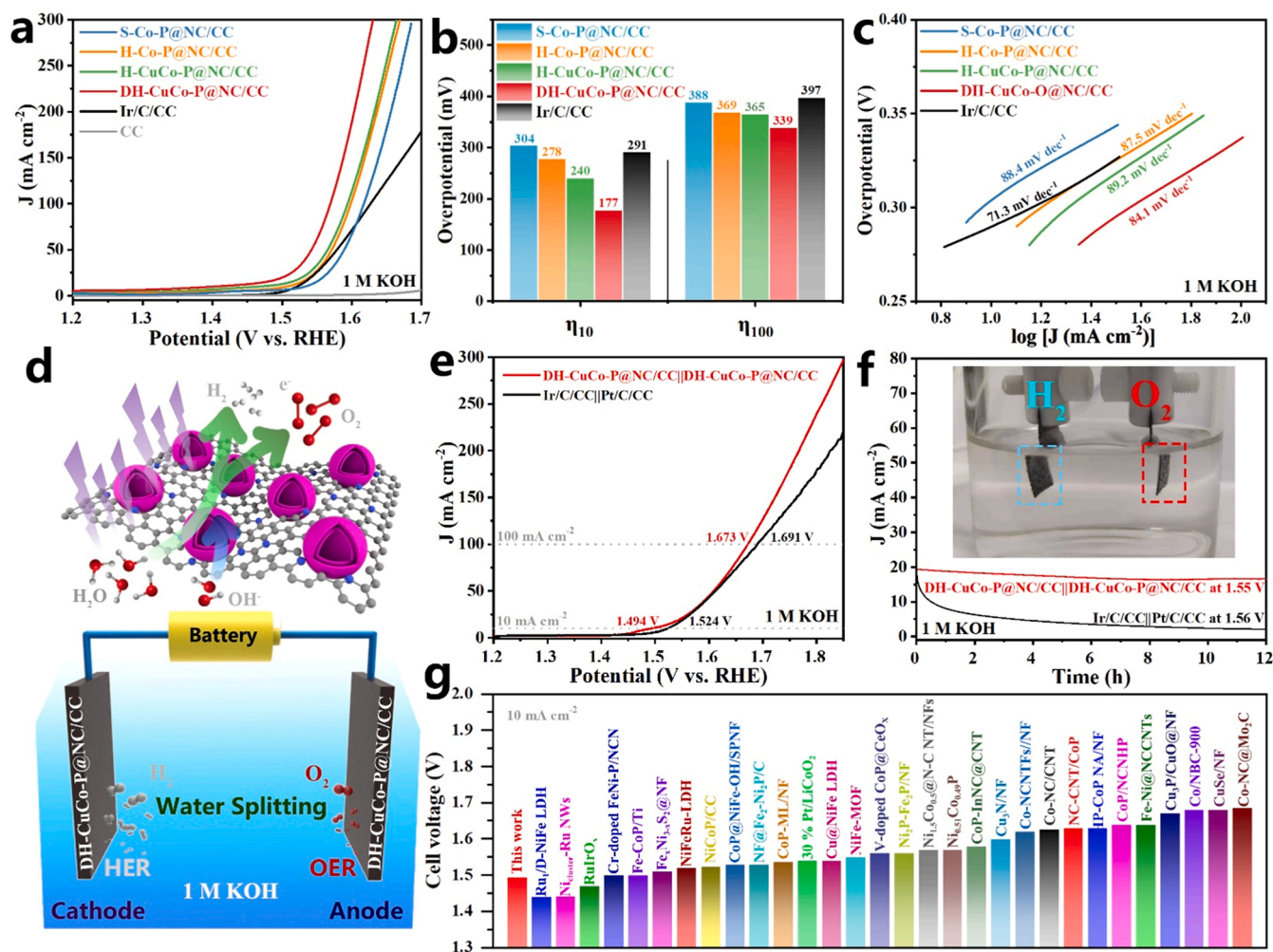


Fig. 6. OER and overall water-splitting performances of various electrocatalysts. (a) LSV curves, (b) comparison of η_{10} and η_{100} , and (c) corresponding Tafel slopes of various electrocatalysts in 1 M KOH solution for OER. (d) The scheme of water splitting mechanism in an electrolyzer based on DH-CuCo-P@NC/CC cathode and anode; (e) LSV curves, and (f) i-t curves at a settled cell voltage for 12 h of DH-CuCo-P@NC/CC || DH-CuCo-P@NC/CC and Ir/C/CC || Pt/C/CC full cells in a two-electrode configuration in 1 M KOH solution; (g) Comparison of the cell voltages to reach 10 mA cm^{-2} with different water electrolyzers in 1 M KOH solution reported by recent literature.

composites. It is obvious that the double-shell hollow NPs in DH-CuCo-P @ NC/CC can provide a faster ion diffusion path and a higher ECSA, thus resulting in its much better HER activity as compared with its solid and single-shell counterparts. Moreover, Figs. 5i and S24–25 show HER stability test results of DH-CuCo-P @ NC/CC in acidic and alkaline media, which confirms the high long-term stability of DH-CuCo-P @ NC/CC as compared with the rapid decay of commercial Pt/CC catalyst after 12 h continuous electrolysis or 1000 CV cycles.

3.6. OER and water splitting performance of electrocatalysts

Subsequently, we further evaluated the OER activity of as-prepared phosphide-contained composites, Ir/C/CC, and CC in a 1.0 M KOH electrolyte. As shown in Fig. 6a–b, DH-CuCo-P @ NC/CC also performs the best OER activity with the smallest $\eta_{10} = 177$ mV and $\eta_{100} = 339$ mV, both of which are much superior to those of H-CuCo-P @ NC/CC ($\eta_{10} = 240$ mV and $\eta_{100} = 365$ mV), H-Co-P @ NC/CC (278 and 369 mV), commercial Ir/C ($\eta_{10} = 291$ mV and $\eta_{100} = 397$ mV), and S-Co-P @ NC/CC ($\eta_{10} = 304$ mV and $\eta_{100} = 388$ mV). Besides, the corresponding Tafel slope of DH-CuCo-P @ NC/CC is calculated to be 84.1 mV dec^{-1} , which is lower than those of other phosphide-contained composites (Fig. 6c), suggesting its optimal OER kinetics [48,49]. And, DH-CuCo-P @ NC/CC also shows a minimum R_{ct} of 1.2Ω among all phosphide-contained composites, revealing that it has the most superior interfacial charge-transfer kinetics and the fastest ion diffusion path (Fig. S21c). Also, the largest C_{dl} of 40.6 mF cm^{-1} for DH-CuCo-P @ NC/CC implies the most active sites it has in all studied phosphide-contained composites (Fig. S26). However, it is discovered that H-CuCo-P @ NC/CC has a smaller C_{dl} but shows a higher OER activity than H-Co-P @ NC/CC, which infers that Cu doping plays a key role to improve the intrinsic activity during the OER process. And, by analyzing the LSV curves normalized by ECSA in Fig. S28c, we further confirm that the Cu-doped catalysts of DH-CuCo-P @ NC/CC and H-CuCo-P @ NC/CC can exhibit better intrinsic activities as compared with H-Co-P @ NC/CC and S-Co-P @ NC/CC. Due to the improvement in intrinsic activity by Cu doping, the optimization of the diffusion path, and the increase of ECSA by unique double-shell hollow structure, the OER activity of DH-CuCo-P @ NC/CC can be greatly boosted. Furthermore, the high durability of DH-CuCo-P @ NC/CC can be also confirmed in Fig. S27a–b, which reveals that the current density of DH-CuCo-P @ NC/CC has almost no obvious degradation after the 12 h of stability test or rapid aging test for 1000 CV cycles, much better than that of Ir/C. In addition, the actual yields of H_2 and O_2 produced by the electrolysis under constant voltage are consistent with the theoretical values, revealing that the Faraday efficiencies of DH-CuCo-P @ NC/CC in the OER and HER processes are both close to 100% (Figs. S24c, S25c, and S27c).

Considering that our self-supported DH-CuCo-P @ NC/CC has an excellent bifunctional activity of HER and OER in alkaline solution, we have further assembled a simple electrolyzer for alkaline overall water splitting by directly using it as both anode and cathode (Fig. 6d). To our delight, the homemade DH-CuCo-P @ NC/CC = |DH-CuCo-P @ NC/CC device only needs a very low cell voltage of 1.494 V to reach the water splitting current density of 10 mA cm^{-2} , which is even 30 mV lower than that of Pt/C/CC = |Ir/C/CC (1.524 V) (Fig. 6e and Movie S1), indicating that the fabrication of double-shell hollow Cu-doped CoP NPs anchored on the carbon nanosheet arrays is an efficient strategy to boost the electrocatalytic kinetics of overall water splitting. Furthermore, as shown in Figs. 6f and S29, the current density of the electrolyzer assembled by DH-CuCo-P @ NC/CC is only slightly attenuated after 12 h of stability test at the voltage of 1.55 V, showing its high durability for overall water splitting in an alkaline condition, which is far superior to commercial Pt/C/CC = |Ir/C/CC electrode couple. As shown in the inset of Fig. 6f, a large number of H_2 and O_2 bubbles can be observed to continuously escape from the surfaces of the two DH-CuCo-P @ NC electrodes during the stability test. Encouragingly, the DH-CuCo-

P @ NC-based electrolyzer only requires the low cell voltage of 1.494 V to reach the current density of 10 mA cm^{-2} and it still has the edge compared with most reported bifunctional electrocatalysts for alkaline overall water splitting (Fig. 6g and Table S1).

Supplementary material related to this article can be found online at doi:10.1016/j.apcatb.2022.122295.

3.7. Characterization of DH-CuCo-P@NC/CC after HER/OER

In addition, by characterizing the used DH-CuCo-P @ NC/CC, its real active sites can be disclosed. By analyzing Fig. S30–32, the XRD characteristic peaks, Raman spectra, and XPS signal peaks of the DH-CuCo-P @ NC/CC after the HER stability test are similar to those of the pristine DH-CuCo-P @ NC/CC. Moreover, SEM and TEM images of the DH-CuCo-P @ NC/CC after the HER stability test (Fig. S33a–c) exhibit that its leaf-shaped carbon nanosheets and double-shell hollow NPs are still maintained. The lattice fringes of 0.248 and 0.189 nm are still consistent with the (111) and (211) planes of CoP in the HRTEM image (Fig. S33c). All these results indicate that the structure of Cu-doped CoP is almost unchanged under the alkaline condition and Cu-doped CoP is always the main active site in the HER process.

However, the structure of the DH-CuCo-P @ NC/CC after the OER stability test has undergone a significant change, since part of Cu-doped CoP has been converted to Cu-doped CoOOH to form the heterostructure of Cu-doped CoOOH/Cu-doped CoP in the OER process. In the XRD pattern of the DH-CuCo-P @ NC/CC after the OER stability test (Fig. S30), a new peak at 20.2° can be observed, which belongs to the (003) plane of CoOOH. And, there are also the diffraction peaks of CoP in the XRD pattern of the DH-CuCo-P @ NC/CC after the OER stability test, suggesting that CoOOH and CoP coexist in it. In addition, two obvious new peaks appear in the Raman spectrum of the DH-CuCo-P @ NC/CC after the OER stability test (Fig. S31), which can be attributed to CoOOH (503 cm^{-1}) and CoO_x (600 cm^{-1}) [50]. Moreover, as shown in Fig. S32, the high-resolution XPS spectra for Co 2p, Cu 2p, O 1s, and P 2p of the DH-CuCo-P @ NC/CC after the OER stability test are also significantly different from those of the pristine DH-CuCo-P @ NC/CC. In particular, the XPS spectra for O 1s of the DH-CuCo-P @ NC/CC after the OER stability test has two new peaks located at 529.7 and 531.0 eV corresponding to the Co-O/Cu-O and Co-OH/Cu-OH species, respectively, which can be attributed to the newly formed Cu-doped CoOOH [51]. In particular, we can see that the DH-CuCo-P @ NC/CC after the OER stability test still maintains its leaf-shaped morphology in Fig. S33d. The TEM images of Fig. S33e–g further reveal the double-shell hollow structure of NPs of the DH-CuCo-P @ NC/CC after the OER stability test can be partially maintained. In the HRTEM image of the DH-CuCo-P @ NC/CC after the OER stability test, there are the lattice fringes with a characteristic spacing of 0.240 nm that belongs to the (101) plane of CoOOH, and another set of lattice fringes with a spacing of 0.189 nm that can be indexed to the (211) plane of CoP in the shell layer of the NP (Fig. S33f). Furthermore, the EDX element mapping images in Fig. S33g exhibit that the Co, Cu, O, and P elements are uniformly distributed in a representative NP of the DH-CuCo-P @ NC/CC after the OER stability test. Through elemental analysis, the Co, Cu, O, and P element contents of the DH-CuCo-P @ NC/CC after the OER stability test are determined to be 40.5 at%, 3.9 at%, 36.2 at%, and 3.8 at%, respectively. This reconfirms that the Cu-doped CoP species can be partially converted into the Cu-doped CoOOH species during OER process, which is also consistent with the reported literature [52]. In addition, by comparing the Co 2p XPS spectrum of the used DH-CuCo-P @ NC/CC with that of the used H-Co-P @ NC/CC (Fig. S34), we can observe a positive-going peak shift of about 0.12 eV for the DH-CuCo-P @ NC/CC after the OER stability test, suggesting that Cu doping adjusts the electronic structure of Co and there is a strong electronic interaction between the Cu and Co in the Cu-doped CoOOH of the DH-CuCo-P @ NC/CC after the OER stability test [53]. According to the above analysis, we can safely infer that the Cu-doped CoOOH is the real

active species for efficient OER, which is also consistent with recently reported literature [54]. In addition, the nitrogen-doped porous carbon is not only a highly conductive substrate to effectively enhance the dispersity of active species, but also changes their electronic structures to facilitate water splitting [55,56]. Above all, benefiting from its favorable Cu doping, high dispersity of metal phosphide, unique double-shell hollow nanostructure, and desirable hierarchical self-supporting porous carbon structure, DH-CuCo-P @ NC/CC has large ECSA, high intrinsic activity, fast diffusion paths, and good conductivity, all of which are responsible for its excellent water splitting performance and long-term stability.

3.8. Density functional theory calculation

Our self-supported DH-CuCo-P @ NC/CC has an excellent OER activity, and its active species can be considered as Cu-CoOOH/Cu-CoP heterostructure that is transformed from the Cu-doped CoP NPs. To gain insights into the effect of the Cu doping in CoOOH and the synergistic effect between Cu-CoOOH and Cu-CoP on improving the intrinsic activity of the catalyst for OER, density functional theory (DFT) calculations are carried out to investigate OER processes. Therefore, three structures including CoOOH (001), Cu-CoOOH (001), and Cu-CoOOH (001)/Cu-CoP (111) are built firstly (Fig. 7a). The optimized adsorption configurations of OH^* on them are exhibited in Fig. 7a, indicating that the surface O atoms connected with metal atoms act as active sites for reactive adsorption. For Cu-CoOOH (001) and Cu-CoOOH (001)/Cu-CoP (111), the surface O atom linked with the doped Cu atom is the optimum adsorption site. The calculated Gibbs free energy for each step is shown in Fig. 7b. The rate-determining step (RDS) of OER on CoOOH (001) is step II $\text{OH}^* \rightarrow \text{O}^* + (\text{H}^+ + \text{e}^-)$, with ΔG_2 of 1.89 V and an overpotential of 0.66 V, well consistent with the previous study [53]. After introducing Cu dopants, the RDS remains unchanged, but the overpotential is decreased to 0.45 V, signifying that Cu doping in CoOOH improves the OER activity. Furthermore, as the experiments observed that the surface Cu-CoOOH is regarded as active species, the synergistic effect between Cu-CoOOH and Cu-CoP heterostructure also may effectively enhance its intrinsic OER activity. Interestingly, the RDS of OER on Cu-CoOOH (001)/Cu-CoP (111) is the step I $\text{H}_2\text{O} (\text{l}) + \text{*} \rightarrow \text{*OH}$

+ $(\text{H}^+ + \text{e}^-)$ with the smallest ΔG_1 of 1.55 V and the overpotential of 0.32 V. Therefore, Cu-CoOOH (001) on Cu-CoP (111) surface is the most prone to OER reaction. It can be also found that the *OH intermediate plays a key role in the OER process among the three kinds of structure. Thus, the adsorption energies of *OH are calculated and displayed in Fig. 7c. Too strong or weak interaction of adsorbates on electrocatalysts could negatively affect the catalytic activity. Obviously, the incorporation of Cu into CoOOH and the heterostructure of Cu-CoOOH with Cu-CoP could decrease the adsorption strength of *OH due to the more positive adsorption energy, thus benefiting the OER process. Overall, the simulated results validate the experimental results regarding the superior intrinsic activity for OER on Cu-CoOOH/Cu-CoP heterostructure derived from partially transformed Cu-doped CoP.

4. Conclusions

To sum up, we have developed a novel strategy to utilize the Kirkendall effect to load leaf-shaped carbon nanosheet arrays with controllable phosphide NPs on a CC substrate, including solid, hollow, and double-shell hollow structure NPs. The formation process and mechanism studies reveal that the intensified Kirkendall effect caused by Cu doping is crucial to forming the double-shell hollow structure. The double-shell hollow structure brings a larger ESCA and a faster diffusion path, enhancing the electrocatalytic performance of DH-CuCo-P @ NC/CC. Furthermore, both the experiment and DFT calculation results confirm that the enhanced OER intrinsic activity of Cu-CoOOH/Cu-CoP heterostructure derived from partially transformed Cu-doped CoP can be attributed to the Cu dopants and the synergistic effect between Cu-CoOOH and Cu-CoP heterostructure. Furthermore, DH-CuCo-P @ NC/CC as a bifunctional self-supported electrocatalyst exhibits excellent and stable water splitting performance in the alkaline electrolyte with a low cell voltage of 1.494 V to reach 10 mA cm^{-2} . This work provides new ideas for adjusting the nanostructure of NPs even in solid media like carbon layers based on the intensified Kirkendall effect for various practical applications such as electrocatalysis, heterogeneous catalysis, etc.

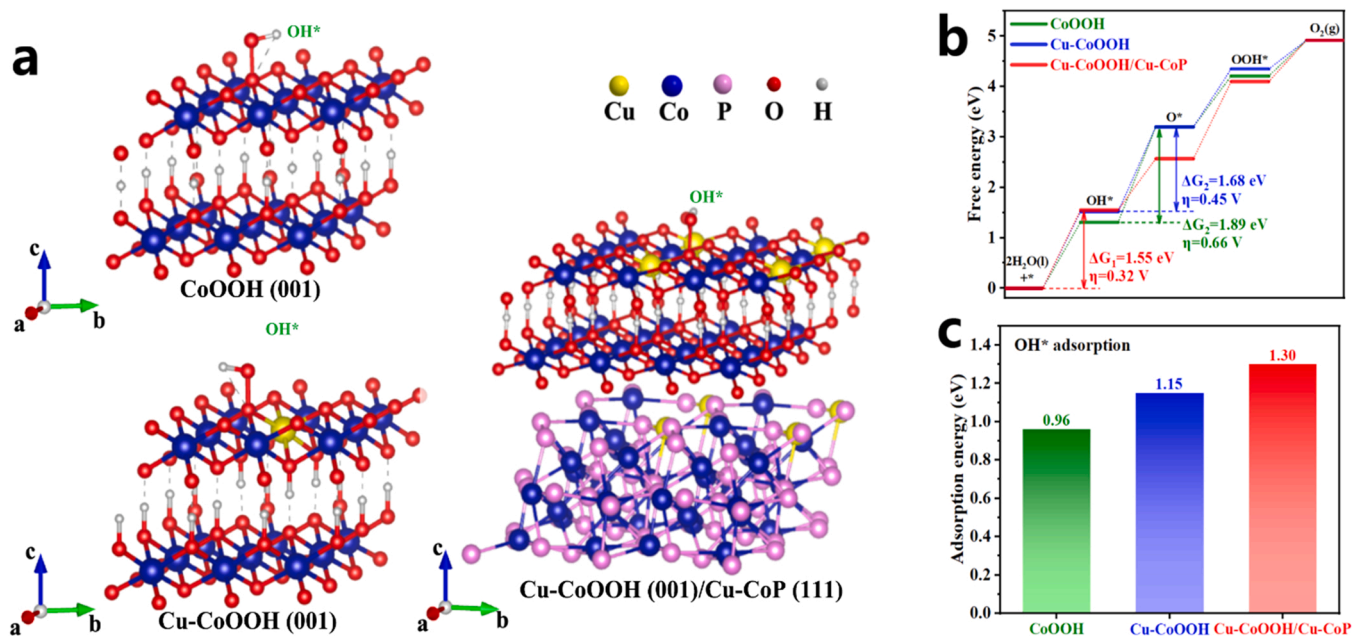


Fig. 7. DFT calculations of CoOOH, Cu-CoOOH, and Cu-CoOOH/Cu-CoP for OER. (a) The optimized adsorption configuration of *OH on CoOOH (001), Cu-CoOOH (001), and Cu-CoOOH (001)/Cu-CoP (111) models. (b) The OER Gibbs free energy diagrams of CoOOH (001), Cu-CoOOH (001), and Cu-CoOOH (001)/Cu-CoP (111) models. (c) The adsorption energy of OH^* on CoOOH (001), Cu-CoOOH (001), and Cu-CoOOH (001)/Cu-CoP (111) models.

CRediT authorship contribution statement

Kui Shen: conceived the idea, designed the experiments, and revised the draft. **Xian Wang:** synthesized, characterized, and tested materials and Writing – original draft. **Haigen Huang:** conceived the idea, designed experiments, synthesized, and characterized materials. **Yingwei Li:** provided many valuable suggestions and discussions. **Jinjie Qian:** provided many valuable suggestions and discussions.

Declaration of Competing Interest

The authors declare that they have no known competing financial interests or personal relationships that could have appeared to influence the work reported in this paper.

Data availability

The authors are unable or have chosen not to specify which data has been used.

Acknowledgments

This work is financially supported by the State Key Laboratory of Pulp and Paper Engineering (2022PY05), and the National Natural Science Foundation of China (22138003 and 21825802). The authors acknowledged the HPC resources provided by the University of Stavanger.

Appendix A. Supplementary material

Supplementary data associated with this article can be found in the online version at doi:10.1016/j.apcatb.2022.122295.

References

- [1] P. De Luna, C. Hahn, D. Higgins, S.A. Jaffer, T.F. Jaramillo, E.H. Sargent, What would it take for renewably powered electrosynthesis to displace petrochemical processes? *Science* 364 (6438) (2019) 3506.
- [2] P. Zhai, M. Xia, Y. Wu, G. Zhang, J. Gao, B. Zhang, S. Cao, Y. Zhang, Z. Li, Z. Fan, C. Wang, X. Zhang, J.T. Miller, L. Sun, J. Hou, Engineering single-atomic ruthenium catalytic sites on defective nickel-iron layered double hydroxide for overall water splitting, *Nat. Commun.* 12 (1) (2021) 4587.
- [3] X. Liu, M. Gong, S. Deng, T. Zhao, T. Shen, J. Zhang, D. Wang, Transforming damage into benefit: corrosion engineering enabled electrocatalysts for water splitting, *Adv. Funct. Mater.* 31 (11) (2020), 2009032.
- [4] X. Zheng, P. Cui, Y. Qian, G. Zhao, X. Zheng, X. Xu, Z. Cheng, Y. Liu, S.X. Dou, W. Sun, Multifunctional active-center-transferable platinum/lithium cobalt oxide heterostructured electrocatalysts towards superior water splitting, *Angew. Chem. Int. Ed.* 59 (34) (2020) 14533–14540.
- [5] G. Zhao, P. Li, N. Cheng, S.X. Dou, W. Sun, An Ir/Ni(OH)₂ heterostructured electrocatalyst for the oxygen evolution reaction: breaking the scaling relation, stabilizing iridium(V), and beyond, *Adv. Mater.* 32 (24) (2020), 2000872.
- [6] T. Liu, P. Li, N. Yao, T. Kong, G. Cheng, S. Chen, W. Luo, Self-sacrificial template-directed vapor-phase growth of MOF assemblies and surface vulcanization for efficient water splitting, *Adv. Mater.* 31 (21) (2019), 1806672.
- [7] T. Guo, L. Chen, Y. Li, K. Shen, Controllable synthesis of ultrathin defect-rich LDH nanoarrays coupled with MOF-derived Co-NC microarrays for efficient overall water splitting, *Small* 18 (29) (2022), 2107739.
- [8] Y. Li, Z. Dong, L. Jiao, Multifunctional transition metal-based phosphides in energy-related electrocatalysis, *Adv. Energy Mater.* 10 (11) (2019), 1902104.
- [9] Y. Lin, L. Yang, Y. Zhang, H. Jiang, Z. Xiao, C. Wu, G. Zhang, J. Jiang, L. Song, Defective carbon-CoP nanoparticles hybrids with interfacial charges polarization for efficient bifunctional oxygen electrocatalysis, *Adv. Energy Mater.* 8 (18) (2018), 1703623.
- [10] Y. Feng, H. Liu, J. Yang, A selective electrocatalyst-based direct methanol fuel cell operated at high concentrations of methanol, *Sci. Adv.* 3 (6) (2017), e1700580.
- [11] Z. Wang, K. Shen, L. Chen, Y. Li, Scalable synthesis of multi-shelled hollow N-doped carbon nanosheet arrays with confined Co/CoP heterostructures from MOFs for pH-universal hydrogen evolution reaction, *Sci. China Chem.* 65 (2021) 619.
- [12] H. Liu, J. Guan, S. Yang, Y. Yu, R. Shao, Z. Zhang, M. Dou, F. Wang, Q. Xu, Metal-organic-framework-derived Co₂P nanoparticle/multi-doped porous carbon as a trifunctional electrocatalyst, *Adv. Mater.* 32 (36) (2020), 2003649.
- [13] X. Wang, Z. Ma, L. Chai, L. Xu, Z. Zhu, Y. Hu, J. Qian, S. Huang, MOF derived N-doped carbon coated CoP particle/carbon nanotube composite for efficient oxygen evolution reaction, *Carbon* 141 (2019) 643–651.
- [14] E. González, J. Arbiol, F. Puentes Víctor, Carving at the nanoscale: sequential galvanic exchange and kirkendall growth at room temperature, *Science* 334 (6061) (2011) 1377–1380.
- [15] M.A. Mahmoud, F. Saira, M.A. El-Sayed, Experimental evidence for the nanocage effect in catalysis with hollow nanoparticles, *Nano Lett.* 10 (9) (2010) 3764–3769.
- [16] X. Sun, G. He, C. Xiong, C. Wang, X. Lian, L. Hu, Z. Li, S.J. Dalgarno, Y.-W. Yang, J. Tian, One-pot fabrication of hollow porphyrinic MOF nanoparticles with ultrahigh drug loading toward controlled delivery and synergistic cancer therapy, *ACS Appl. Mater. Interfaces* 13 (3) (2021) 3679–3693.
- [17] Q. Sun, N. Wang, J. Yu, J.C. Yu, A hollow porous CdS photocatalyst, *Adv. Mater.* 30 (45) (2018), 1804368.
- [18] J. Park, T. Kwon, J. Kim, H. Jin, H.Y. Kim, B. Kim, S.H. Joo, K. Lee, Hollow nanoparticles as emerging electrocatalysts for renewable energy conversion reactions, *Chem. Soc. Rev.* 47 (22) (2018) 8173–8202.
- [19] M. Fan, D. Liao, M.F.A. Aboud, I. Shakir, Y. Xu, A universal strategy toward ultrasmall hollow nanostructures with remarkable electrochemical performance, *Angew. Chem. Int. Ed.* 59 (21) (2020) 8247–8254.
- [20] S.L. Zhang, B.Y. Guan, X.W.D. Lou, Co-Fe alloy/N-doped carbon hollow spheres derived from dual metal-organic frameworks for enhanced electrocatalytic oxygen reduction, *Small* 15 (13) (2019), 1805324.
- [21] T. He, X. Xu, B. Ni, H. Lin, C. Li, W. Hu, X. Wang, Metal-organic framework based microcapsules, *Angew. Chem. Int. Ed.* 57 (32) (2018) 10148–10152.
- [22] B. Wang, H.B. Wu, L. Zhang, X.W. Lou, Self-supported construction of uniform Fe₃O₄ hollow microspheres from nanoplate building blocks, *Angew. Chem. Int. Ed.* 52 (15) (2013) 4165.
- [23] D. Ding, K. Shen, X. Chen, H. Chen, J. Chen, T. Fan, R. Wu, Y. Li, Multi-level architecture optimization of MOF-templated Co-based nanoparticles embedded in hollow N-doped carbon polyhedra for efficient OER and ORR, *ACS Catal.* 8 (9) (2018) 7879–7888.
- [24] X. Wang, A. Dong, Z. Zhu, L. Chai, J. Ding, L. Zhong, T.T. Li, Y. Hu, J. Qian, S. Huang, Surfactant-mediated morphological evolution of MnCo Prussian Blue structures, *Small* 16 (43) (2020), 2004614.
- [25] Z. Yang, N. Yang, J. Yang, J. Bergström, M.-P. Pileni, Control of the oxygen and cobalt atoms diffusion through Co nanoparticles differing by their crystalline structure and size, *Adv. Funct. Mater.* 25 (6) (2015) 891–897.
- [26] Y. Tang, S. Chen, S. Mu, T. Chen, Y. Qiao, S. Yu, F. Gao, Synthesis of capsule-like porous hollow nanonickel cobalt sulfides via cation exchange based on the Kirkendall effect for high-performance supercapacitors, *ACS Appl. Mater. Interfaces* 8 (15) (2016) 9721–9732.
- [27] Q. Wang, Z. Zhang, C. Cai, M. Wang, Z.L. Zhao, M. Li, X. Huang, S. Han, H. Zhou, Z. Feng, L. Li, J. Li, H. Xu, J.S. Francisco, M. Gu, Single iridium atom doped Ni₂P catalyst for optimal oxygen evolution, *J. Am. Chem. Soc.* 143 (34) (2021) 13605–13615.
- [28] R.-K. Chiang, R.-T. Chiang, Formation of hollow Ni₂P nanoparticles based on the nanoscale Kirkendall effect, *Inorg. Chem.* 46 (2) (2007) 369–371.
- [29] A.E. Henkes, Y. Vasquez, R.E. Schaak, Converting metals into phosphides: a general strategy for the synthesis of metal phosphide nanocrystals, *J. Am. Chem. Soc.* 129 (7) (2007) 1896–1897.
- [30] H. Tianou, W. Wang, X. Yang, Z. Cao, Q. Kuang, Z. Wang, Z. Shan, M. Jin, Y. Yin, Inflating hollow nanocrystals through a repeated Kirkendall cavitation process, *Nat. Commun.* 8 (1) (2017) 1261.
- [31] M. Xie, Z. Lyu, R. Chen, M. Shen, Z. Cao, Y. Xia, Pt-Co@Pt octahedral nanocrystals: enhancing their activity and durability toward oxygen reduction with an intermetallic core and an ultrathin shell, *J. Am. Chem. Soc.* 143 (22) (2021) 8509–8518.
- [32] J. Ding, T. Fan, K. Shen, Y. Li, Electrochemical synthesis of amorphous metal hydroxide microarrays with rich defects from MOFs for efficient electrocatalytic water oxidation, *Appl. Catal. B Environ.* 292 (2021), 120174.
- [33] D.J.H. Cant, C. Minelli, K. Sparnacci, A. Müller, H. Kalbe, M. Stöger-Pollach, W.E. S. Unger, W.S.M. Werner, A.G. Shard, Surface-energy control and characterization of nanoparticle coatings, *J. Phys. Chem. C* 124 (20) (2020) 11200–11211.
- [34] G. Ouyang, C.X. Wang, G.W. Yang, Surface energy of nanostructured materials with negative curvature and related size effects, *Chem. Rev.* 109 (9) (2009) 4221–4247.
- [35] K.-Y. Niu, J. Park, H. Zheng, A.P. Alivisatos, Revealing bismuth oxide hollow nanoparticle formation by the Kirkendall effect, *Nano Lett.* 13 (11) (2013) 5715–5719.
- [36] W. Wang, M. Dahl, Y. Yin, Hollow nanocrystals through the nanoscale Kirkendall effect, *Chem. Mater.* 25 (8) (2013) 1179–1189.
- [37] Z. Yang, N. Yang, M.-P. Pileni, Nano Kirkendall effect related to nanocrystallinity of metal nanocrystals: influence of the outward and inward atomic diffusion on the final nanoparticle structure, *J. Phys. Chem. C* 119 (39) (2015) 22249–22260.
- [38] Z.H. Xue, H. Su, Q.Y. Yu, B. Zhang, H.H. Wang, X.H. Li, J.S. Chen, Janus Co/CoP nanoparticles as efficient Mott-Schottky electrocatalysts for overall water splitting in wide pH range, *Adv. Energy Mater.* 7 (12) (2017), 1602355.
- [39] A. Han, H. Zhang, R. Yuan, H. Ji, P. Du, Crystalline copper phosphide nanosheets as an efficient janus catalyst for overall water splitting, *ACS Appl. Mater. Interfaces* 9 (3) (2017) 2240–2248.
- [40] I. Lorite, J.J. Romero, J.F. Fernández, Effects of the agglomeration state on the Raman properties of Co₃O₄ nanoparticles, *J. Raman Spectrosc.* 43 (10) (2012) 1443–1448.
- [41] D. Ji, L. Fan, L. Tao, Y. Sun, M. Li, G. Yang, T.Q. Tran, S. Ramakrishna, S. Guo, The Kirkendall effect for engineering oxygen vacancy of hollow Co₃O₄ nanoparticles toward high-performance portable zinc-air batteries, *Angew. Chem. Int. Ed.* 58 (39) (2019) 13840–13844.

- [42] Z. Liang, C. Qu, W. Zhou, R. Zhao, H. Zhang, B. Zhu, W. Guo, W. Meng, Y. Wu, W. Aftab, Q. Wang, R. Zou, Synergistic effect of Co-Ni hybrid phosphide nanocages for ultrahigh capacity fast energy storage, *Adv. Sci.* 6 (8) (2019), 1802005.
- [43] R. Wang, X.Y. Dong, J. Du, J.Y. Zhao, S.Q. Zang, MOF-derived bifunctional Cu₃P nanoparticles coated by a N, P-codoped carbon shell for hydrogen evolution and oxygen reduction, *Adv. Mater.* 30 (6) (2018), 1703711.
- [44] S. Liu, L. Cui, S. Yin, H. Ren, Z. Wang, Y. Xu, X. Li, L. Wang, H. Wang, Heterointerface-triggered electronic structure reformation: Pd/CuO nano-olives motivate nitrite electroreduction to ammonia, *Appl. Catal. B Environ.* 319 (2022), 121876.
- [45] X. Wang, Y. Du, L. Chai, J. Ding, L. Zhong, T. Miao, Y. Hu, J. Qian, S. Huang, Sulfur-induced growth of coordination polymer-derived straight carbon nanotubes on carbon nanofiber network for Zn-air batteries, *Chem. Eur. J.* 27 (2021) 7704–7711.
- [46] L. Yang, R. Liu, L. Jiao, Electronic redistribution: construction and modulation of interface engineering on CoP for enhancing overall water splitting, *Adv. Funct. Mater.* 30 (14) (2020), 1909618.
- [47] T. Zhu, S. Liu, B. Huang, Q. Shao, M. Wang, F. Li, X. Tan, Y. Pi, S.-C. Weng, B. Huang, Z. Hu, J. Wu, Y. Qian, X. Huang, High-performance diluted nickel nanoclusters decorating ruthenium nanowires for pH-universal overall water splitting, *Energy Environ. Sci.* 14 (5) (2021) 3194–3202.
- [48] X. Wang, L. Chai, J. Ding, L. Zhong, Y. Du, T.-T. Li, Y. Hu, J. Qian, S. Huang, Chemical and morphological transformation of MOF-derived bimetallic phosphide for efficient oxygen evolution, *Nano Energy* 62 (2019) 745.
- [49] L. Yan, B. Zhang, J. Zhu, Y. Li, P. Tsiakaras, P. Kang Shen, Electronic modulation of cobalt phosphide nanosheet arrays via copper doping for highly efficient neutral-pH overall water splitting, *Appl. Catal. B Environ.* 265 (2020), 118555.
- [50] T.I. Singh, G. Rajeshkhanna, U.N. Pan, T. Kshetri, H. Lin, N.H. Kim, J.H. Lee, Alkaline water splitting enhancement by MOF-derived Fe-Co-Oxide/Co@NC-mNS heterostructure: boosting OER and HER through defect engineering and in situ oxidation, *Small* 17 (29) (2021), 2101312.
- [51] S.H. Ye, Z.X. Shi, J.X. Feng, Y.X. Tong, G.R. Li, Activating CoOOH porous nanosheet arrays by partial iron substitution for efficient oxygen evolution reaction, *Angew. Chem. Int. Ed.* 57 (10) (2018) 2672–2676.
- [52] H. Xie, C. Lan, B. Chen, F. Wang, T. Liu, Noble-metal-free catalyst with enhanced hydrogen evolution reaction activity based on granulated Co-doped Ni-Mo phosphide nanorod arrays, *Nano Res.* 13 (12) (2020) 3321–3329.
- [53] L. Yan, B. Zhang, Z. Liu, J. Zhu, Synergy of copper doping and oxygen vacancies in porous CoOOH nanoplates for efficient water oxidation, *Chem. Eng. J.* 405 (2021), 126198.
- [54] R. Zhang, Z. Wei, G. Ye, G. Chen, J. Miao, X. Zhou, X. Zhu, X. Cao, X. Sun, “d-Electron complementation” induced V-Co phosphide for efficient overall water splitting, *Adv. Energy Mater.* 11 (38) (2021), 2101758.
- [55] X.Z. Fan, X. Du, Q.Q. Pang, S. Zhang, Z.Y. Liu, X.Z. Yue, In situ construction of bifunctional N-doped carbon-anchored Co nanoparticles for OER and ORR, *ACS Appl. Mater. Interfaces* 14 (6) (2022) 8549–8556.
- [56] D. Zhao, K. Sun, W.C. Cheong, L. Zheng, C. Zhang, S. Liu, X. Cao, K. Wu, Y. Pan, Z. Zhuang, B. Hu, D. Wang, Q. Peng, C. Chen, Y. Li, Synergistically interactive pyridinic-N-MoP sites: identified active centers for enhanced hydrogen evolution in alkaline solution, *Angew. Chem. Int. Ed.* 59 (23) (2020) 8982–8990.